Metal impurity-assisted formation of nanocone arrays on Si by low energy ion-beam irradiation

Kayla Steeves Lloyd [1], Igor L. Bolotin[1], Martina Schmeling[2], Luke Hanley[1], and Igor V. Veryovkin [1, *]

[1] Department of Chemistry, University of Illinois at Chicago, Chicago, IL 60607

[2] Department of Chemistry and Biochemistry, Loyola University Chicago, Chicago, IL 60626

[*] Corresponding author

Keywords
Ion beam sputtering, Nanoscale morphology evolution, Self-organization
Atomic Force Microscopy, Total Reflection X-ray Spectrometry

Abstract

Fabrication of nanocone arrays on Si surfaces was demonstrated using grazing incidence irradiation with 1 keV Ar^+ ions concurrently sputtering the surface and depositing metal impurity atoms on it. Among three materials compared as co-sputtering targets Si, Cu and stainless steel, only the steel was found to assist the growth of dense arrays of nanocones at ion fluences between 10^{18} and 10^{19} ions/cm^2. The structural characterization of samples irradiated with these ion fluences using Scanning Electron Microscopy and Atomic Force Microscopy revealed that regions far away from co-sputtering targets are covered with nanoripples, and that nanocones popped-up out of the rippled surfaces when moving closer to co-sputtering targets, with their density gradually increasing and reaching saturation in the regions close to these targets. The characterization of the samples' chemical composition with Total Reflection X-ray Fluorescence Spectrometry and X-ray Photoelectron Spectroscopy revealed that the concentration of metal impurities originating from stainless steel (Fe, Cr and Ni) was relatively high in the regions with high density of nanocones (Fe reaching a few atomic percent) and much lower (factor of 10 or so) in the region of nanoripples. Total Reflection X-ray Fluorescence Spectrometry measurements showed that higher concentrations of these impurities are accumulated under the surface in both regions. X-ray Photoelectron Spectroscopy experiments showed no direct evidence of metal silicide formation occurring on one region only (nanocones or nanoripples) and thus showed that this process could not be the driver of nanocone array formation. Also, these measurements indicated enhancement in oxide formation on regions covered by nanocones. Overall, the results of this study suggest that the difference in concentration of metal impurities in the thin near-surface layer forming under ion irradiation might be responsible for the differences in surface structures.

Metal impurity-assisted formation of nanocone arrays on Si by low energy ion-beam irradiation

Kayla Steeves Lloyd [1], Igor L. Bolotin[1], Martina Schmeling[2], Luke Hanley[1], and Igor V. Veryovkin [1, *]

[1] Department of Chemistry, University of Illinois at Chicago, Chicago, IL 60607

[2] Department of Chemistry and Biochemistry, Loyola University Chicago, Chicago, IL 60626

[*] Corresponding author

1. Introduction

Interest in using low-energy ion-beam irradiation as a tool for nanostructuring and functionalization of the surfaces of various materials has steadily increased over the last four decades [1-10]. This interest stems in large part from the simplicity and versatility of this technique and its ability to facilitate the fabrication of a rich variety of patterns on solid surfaces [11]. These patterns include ordered arrays of nanoripples [8, 12-15], nanodots [16], nanocones [17], nanoparticles [18, 19] and nanowires [19-21]. Another valuable asset of this technique is the potential to fabricate homogenously ordered nanopatterns over large areas while still maintaining a high degree of control over surface morphology and chemistry [3]. It is widely agreed that the formation of nanopatterns under low-energy ion-beam irradiation occurs via self-organization of the irradiated surface [4, 5, 10, 22-24]. This self-organization phenomenon allows for an effective "bottom-up" approach for nanofabrication [9, 25]. Additionally, by varying the ion irradiation parameters and target temperature, one can control the complex process of surface self-organization and thus enable programmable functionality in materials [9]. This programmable functionality has helped identify numerous applications for such nanostructures, including optimizing the performance of thermoelectric generators, nanosensors, field emitter arrays, and optoelectronic devices [26-28].

Despite the empirical success of nanopattern fabrication, the fundamental understanding of the mechanisms governing pattern selection under ion beam irradiation is still lacking. Existing theoretical models account for early stages of the pattern formation, but these theories do not extend to later stages and therefore require further exploration [29-32]. Additionally, these

same theories fail to predict, for instance, differences in patterns observed for different materials, particularly for chemical compounds [1, 9, 10, 24, 33]. This limitation may have arisen from a focus on surface morphology rather than on surface chemical composition [34]. Recently, interest in surface chemistry has been renewed through the revelation that metal impurities might play a major role in the nanoripple pattern formation [35]. This interest has further grown with the development of so-called surfactant sputtering as evidenced by recent studies of the role of metal impurities in nanopatterns formation [7, 26, 36-38]. Surfactant sputtering, based on the co-deposition of surfactant atoms from a nearby metal target during ion irradiation, can form a variety of the aforementioned patterns on Si surfaces [2, 3, 5, 27, 36, 37, 39]. As a result, a hypothesis that formation of silicides is a necessary condition for pattern formation on silicon recently started to gain broad support [40]. This hypothesis has inspired new studies exploring surface silicide formation during ion irradiation [9, 25, 40-43].

In view of this growing interest in the role of surface impurities in nanopattern formation under low-energy ion irradiation, we report here experimental results of our study of surface nanopattern formation on silicon irradiated by low-energy argon ions that co-sputtered stainless steel targets. Instead of focusing on previously well-studied fine nanoripple and nanodot patterns, this work concentrates on coarser nanostructures, often called arrays of nanocones (sometimes alternatively referred to as nanotips, nanofibers, or nanograss) [44-46]. Nanocones are commonly seen structures obtained with low-energy ion irradiation [9, 17, 26, 46-52]. Moreover, nanostructures with very similar morphology and dimensions can also be produced by plasma-based methods [45, 53, 54]. Nanocones are not exclusive to silicon: metals [47, 48, 50], carbon and other carbonaceous materials [46, 49] including diamond [55], as well as GaSb [56] have also been reported as surfaces where such structures could be fabricated by ion irradiation. Interestingly, the observations that formation of nanocones on ion-irradiated surface can be aided by co-deposition of impurity atoms were made already in 1970s [47-49]. As a possible explanation for this phenomenon, a formation of seed clusters on the surface from impurity atoms due to their surface diffusion was proposed [57], and the apparent consensus in the 1970s literature was that such clusters could locally alter sputtering yield and act as surface masks initiating nanocone formation [47-50].

In this paper we specifically describe ion-irradiated nanostructured samples that have been

comprehensively characterized by structure-sensitive (Scanning Electron Micsoscopy, SEM and Atomic Force microscopy, AFM) and chemical composition-sensitive (X-ray Photoelectron Spectrometry, XPS and Total Reflection X-ray Fluorescence Spectrometry, TXRF) surface characterization techniques in order to better understand the interplay between the chemical composition of these materials and the structure of their surfaces. One of the key questions we asked was whether the silicide formation was indeed the primary driver of the surface self-organization in this case, especially in view of others reporting the same structures forming on diamond and other materials irradiated by low energy ions [40, 46, 56].

2. Experimental details

The instrumentation used in this work for ion bombardment and X-ray photoelectron analysis has been previously described [58-60]. The ion irradiation layout can be seen in Figure 1. Briefly, a commercial Kaufman ion source (Fig. 1a) using electron impact ionization (Model 3 cm Ion Source, Veeco-CS) produced 1 keV Ar^+ ions, with working pressure of Ar gas (99.99% purity) maintained by a mass flow controller (Type 246, MKS). Si wafers (Wafer World, Inc., Si (100) p-type, boron doped) were used as irradiation targets for all experiments (Fig. 1b). The irradiation chamber had a base pressure of 4×10^{-9} Torr and working pressure of 3×10^{-5} Torr. The sample fabrication was carried out at an ion incident angle of 75° off normal with near-grazing incidence, with a distance between ion source and the target of ~200 mm. The typical average ion current density was 1 $\mu A/mm^2$ for the beam profile with FWHM of approximately 20 mm. The samples discussed here were irradiated at room temperature for periods of time between 40 and 120 minutes corresponding to ion fluences of ~3×10^{18} ions/cm^2 and 9×10^{18} ions/cm^2, respectively. Before and after each sample irradiation, a Faraday cup was utilized to measure ion beam profile by scanning across the beam. Although generally stable, the primary ion current exhibited a slow drift during a given measurement.

Prior to irradiation with Ar^+ ions, samples were mounted onto a custom-built sample holder as seen in Fig. 1b. In the diagram provided, ions are approaching the target downwards from the right. The ridges on the sample plate were made such that co-sputtering targets could be interchanged for different materials (stainless steel, Cu, Si, etc.) or, alternatively, the ridges themselves can serve as targets. The angle between the ridge and sample surface was

approximately 45°. The material used to fabricate the ridges was 302 stainless steel shim stock with thickness 127 μm (0.005”), which after bending to the desired angle was spot-welded on the main sample holder plate. The ion beam simultaneously irradiated both the sample and the co-sputtering target, thereby allowing for irradiation and concurrent metal deposition onto the Si sample, as seen in Figs. 1a and 1b. As shown in Fig.1b, we used “sacrificial” Si wafers to shield our samples from material sputtered from the main sample holder: the samples were mounted on top of such wafers, and a separate wafer was installed on the side from which ions approached the samples.

After ion irradiation, the sample has prominent matte areas, which correspond to areas that have been nanostructured (Fig.1c). These areas appear asymmetric because the matte region A was closer to the central ridge where ion current was higher and the ion beam incidence was not perfectly parallel to the ridges so that part of the matte region opposite to region A was in the shade of the ridge (see Fig.1b). Furthermore, the indicated points A and B correspond to the approximate regions characterized by SEM, AFM, TXRF and XPS.

The surface morphology was analyzed by scanning electron microscope (SEM, JEOL JSM-6320F) and atomic force microscope (AFM, Bruker-Nano Dimension Icon). AFM was utilized in contact mode, in air, with a resolution of 512×512 pixels. Cantilevers comprised of silicon nitride and a nominal tip radius of 2 nm were used. The sample was traversed from edge to edge with scans roughly 2 mm apart. For SEM, the samples were examined at 3.2 kV with the same scanning pattern.

Surface elemental concentrations were quantified by Total Reflection X-ray Fluorescence spectrometry, (TXRF, S2PicoFox, Bruker Nano, Berlin) with the aid of calibration curves for each element of interest. To our knowledge, the technique of TXRF has not been applied yet to characterization of surfaces nanostructured by ion beams. Its basic X-ray probe layout is similar to another technique, which was applied to such samples quite often, Grazing Incidence X-ray Scattering (GISAX) [7, 34, 35, 37, 61, 62]. The difference between these two method lies in the type and nature of X-ray detectors used. We chose laboratory-based TXRF because this technique is capable of (1) quantitatively measuring the surface composition and (2) semi-quantitatively probing the elemental composition under the sample surface [63-65]. In TXRF,

a primary X-ray beam (Mo-Anode, 50kV, 600μA) strikes a highly reflective surface at very low incident angles and is totally reflected within the upper few atomic layers of the material. Material deposited on top of the reflective surface or embedded within a few atomic layers below the surface is excited fluorescence and analyzed. Detection limits as low as 10^9 atoms/cm^2 can be achieved with TXRF for heavier elements [63-65]. Analysis time was 2000 seconds for both sample and calibration standards. For quantifying the elemental composition, a multistandard (Cr, Mn, Fe, Ni and Cu - 10 μl of each) solution pipetted on a SiO_2 sample was used, and a special calibration curve was constructed for each element on a Si sample. In order to probe different sample regions, the sample was moved laterally with respect to the fixed position of the X-ray probe, which had a footprint of ~2 mm × 5 mm on the sample surface. In order to perform angular scans of the X-ray beam incidence, the sample was tilted in the beam incidence plane around the center of the X-ray beam spot.

Chemical states of the elements detected on sample surfaces were characterized by high-resolution monochromatic X-ray photoelectron spectroscopy (XPS), using a previously described instrument [59]. A high-resolution monochromatic Al Kα X-ray source (15 keV, 20 mA emission current, model VSW MX10 with a 700 mm Rowland circle monochromator, VSW Ltd., Macclesfield, U.K.) and a 150-mm concentric hemispherical analyzer (model class 150, VSW Ltd.) with a multichannel detector operated at the constant energy pass analyzer mode were used. Selected peak scans were performed with a pass energy of 22 eV. All core level spectra were charge referenced to C 1s, taken to be at 285.0 eV, and fitted using XPS software (XPS PEAK FIT 4.1). Studies were performed such that the surface of the nanopatterned wafer was “mapped” systematically by XPS. Scans were performed laterally across the sample in roughly 1-mm increments from edge to edge. While traversing the sample, survey and core levels were scanned for all relevant components.

3. Results and discussion

Three target materials were investigated for their co-sputtering abilities: stainless steel (SS), copper (Cu), and silicon (Si). The irradiation time was increased in increments of 20 minutes, up to 120 minutes. Only the SS targets produced our pattern of interest (i.e. arrays of nanocones) with these irradiation times. This outcome is commensurate with other results in the field [2, 38]. For Si co-sputtering targets, this is easy to interpret because Si atoms co-deposited on ion irradiated Si surfaces become virtually indistinguishable from Si atoms sputtered from these surfaces, and they diffuse over the surface together as one ensemble. But this was somewhat surprising for Cu atoms that could diffuse as impurity over ion-irradiated Si surface and form clusters seeding nanocone formation [57]. We think of two possible explanations of this observation: (1) under particular conditions of experiments discussed here, either the Ar^+ ion fluence or the flux of co-sputtered Cu atoms could be insufficient to trigger any noticeable nanocone formation - if we accept the mechanism of nanocone formation from 1970s [47-50, 57], and/or (2) Cu atoms did not react with Si surface in the same way and with the same rates as those from SS (Fe, Cr, and Ni) – if we accept that surface silicide formation played a key role here [9, 25, 40-43]. Thus it is apparent that more systematic future studies are needed to help clarify which mechanism is prevalent here and for which set of materials combination and experimental conditions. As for experiments with SS targets, which we are going to discuss below, the lowest irradiation time found to produce nascent *arrays* of nanocones was 40 minutes (i.e. ion fluence of $\sim 3 \times 10^{18}$ ions/cm^2). This time served as a baseline for studying nanocones. Optical examination of the sample regions that contained nanocones revealed that they were distinctly matte appearing unequivocally different from the native shiny, reflective Si surfaces.

3.1 Characterization of surface morphology

The surface morphology of the samples was first characterized *ex situ* by SEM, and some selected images are featured in Figures 2a-2d. SEM imaging corroborated that these matte areas did indeed correspond to arrays of nanocones. Only the peripheral regions close to the ridges with co-sputtering targets were wholly covered in nanocones. However, longer irradiation times facilitated the proliferation of regions with nanocone arrays across the sample,

which was manifested in a widening of the optically matte areas. The density of nanocones gradually increased from none on the unaltered Si surface farthest from the ridges into apparent saturation occurring in the matte regions near the ridges. This finding undoubtedly correlated with the amount of material co-sputtered from the metal targets and deposited onto the surface. Additionally, SEM demonstrated the cones to be on the order of up to a few hundreds of nm in length. The orientation of these cones was angled in the ion incidence plane and towards the ion incidence direction, as schematically depicted in Fig. 2e.

After the SEM characterization, the AFM was used to attain higher lateral resolution in three dimensions. Figs. 3 a-e correspond to a line scan traversing a 100 minute sample (along the A to B line shown on Fig. 1c) in order to observe the transitory development of its surface morphology. The variations in Ar^+ ion fluence over the sample surface due to the ion beam profile (estimated to be about 10% across the whole sample) were apparently a minor factor compared to the distance for each point on the sample from the SS target used for co-sputtering. This is evidenced by the appearance of this particular sample (Fig. 1c), which contained two matte regions on the periphery, as explained above. These two regions with nanocone arrays in the vicinity to ridges with co-sputtering SS targets clearly indicate that it was the flux of metal atoms from SS target which drove the surface morphology development. Similar conclusions on the role of metal co-sputtering targets were earlier reported for nanopattern formation in surfactant sputtering regime [2, 3, 5, 6, 27, 28, 39, 40, 42].

The density of nanocones varies from a region where they were essentially non-existent (Fig. 3a) to regions with moderate density (Figs. 3b) and ultimately to regions where the density increases (Fig. 3c) and saturates (Figs. 3d on one end and Fig. 3e on the other end). The higher lateral resolution of AFM helped to reveal that the nanocone-free region in the center of the sample (Fig. 3a) actually displayed some nanoripple structures where the ripples were oriented parallel to the ion beam incidence. Moreover, closer examination of regions of Figs. 3b and 3c suggests that the nanocones popped out of nanorippled base surface, appearing as randomly distributed “spikes”. This kind of surface evolution appears to be different from the one described recently in Ref. [66] and named “ripple coarsening”. In our case, the “coarsening” actually did not occur until the density of nanocones reached apparent saturation in Fig. 3d. In fact, the comparison between these regions and the corresponding Fig. 3e on the other end of

the sample reveals such a coarsening phenomenon. Other mechanisms known to produce similar surface morphology by transitions from ripples to faceted structure [67, 68] also do not seem to apply to our case because we did not observe a smooth transition but rather an abrupt "pop-up", as shown in Figure 4a, zooming on such a region on Figure 1c . This observation brings us back to consideration of the mechanism of impurity atoms diffusion and seed cluster formation [57] proposed in 1970s, with a key difference that these atoms have to diffuse over nanorippled surfaces. The average size of nanocones on the "saturated" region is several hundreds of nanometers. Figure 4b displays a fine, "grooved" structure aligned along the coarsened nanocone, as if these larger "chunks" of surface are self-organizing on their own. Thus, these nanocone arrays might be called a ***nanostructured mesostructure***, whereby the mesostructure is the array itself, and nanostructures are its components (individual cones).

The nanostructures fabricated in this work resemble the ones reported earlier [69] for similar irradiation conditions with grazing incidence angle but with one key difference. Namely, co-sputtering targets were **not** used in Ref. [69], specifically, "to avoid recording pattern formation due to incorporation of impurities originating from the sample and re-deposition of silicon atoms originating from the sacrificial wafer". However, the experimental details provided in Ref. [69] suggest some metal impurity deposition may have occurred inadvertently because the particular ion source used in these experiments typically implements solid Mo grids for ion extraction, with the outermost grid experiencing significant sputtering erosion. Thus, the formation of nanocone arrays reported in Ref. [69] could quite possibly be assisted by a metal impurity deposition process. If so, then our observations agree very well with the results of that work.

3.2 Characterization of surface chemical composition

In order to better understand and quantify the influence of the metal impurity deposition on the nanocone array formation, we employed two complementary analytical techniques, TXRF and XPS, capable of probing elemental composition of the surface and chemical states of these elements, respectively.

Fig. 5 depicts the layout of mapping the surface composition with angular scans of X-ray probe on different regions of the sample. Fig. 6 compares X-ray fluorescence spectra acquired with

such angular scans on regions A (nanostructured surface containing nanocone arrays) and B (smoother surface covered with nanoripples) while Table 1 lists concentrations of some elements identified in the spectra. Note that the incidence of the X-ray probe beam was chosen to be along the tilt direction of the nanocones in order to better maintain grazing incidence conditions. Among the detected elements, some were corresponding to blank values originating from the irradiation of the vacuum chamber walls (very likely Pb) or from the ion source filament, and plasma cup and grids materials (possibly Zn and Mn), while others - to the sample preparation and handling (e.g. Cu from copper SEM adhesive tape used for mounting samples or Ca, which is generally very abundant in the environment). Argon detected in the sample was coming both from the laboratory air (TXRF is performed at atmospheric pressure) and from the sample (Ar "subplanted" [70, 71] in the topmost few nm, as evidenced by the angular scan when Ar concentration was apparently increasing while increasing the X-ray incidence angle). Other detected elements correspond to the stainless steel used as co-sputtering target (Fe, Cr, and Ni). The angular scans with TXRF (when the incidence angle of X-rays was varied) revealed that concentrations of these elements measured at critical angle (i.e. on the surface) were lower than those at higher angles, suggesting that these metal atoms are buried under the Si surface via ion mixing [72-74]. This makes sense, especially if one imagines that, at some ion irradiation stage, a steady state is reached such that the topmost surface is sputter-eroded by the ion beam, and some of the continuously supplied by the same beam metal impurity atoms are "pushed" under the surface by collisions with primary ions (phenomenon known as knock-on subplantation [75, 76]). What is interesting (see Table 1) is that surface concentrations of all these metal elements are up to an order of magnitude higher on the nanocone array covered region A than on the nanorippled region B. For the region A, atomic concentrations of these elements reach a few percent, as follows. If we estimate surface concentration of Si atoms as 1.4×10^{15} at/cm^2 then the concentration of Fe with its 6.8×10^{13} at/cm^2 is 5%, and Cr with 2.1×10^{12} at/cm^2 is 1.5%. In contrast to this, for the region B, Fe would be only about 0.3% and Cr would be too close to the noise level to allow quantification.

The surface morphology of nanocone arrays fabricated in this work is anisotropic - cones were tilted in the direction from which the ion beam was coming – leading us to anticipate some anisotropy in the TXRF measurements as well. Figure 7 compares TXRF spectra measured on the surface region A with two orientations of the X-ray beam, one coming from the same

direction as the ion beam (i.e. against the nanocone tilt) and the other opposite to it (i.e along the nanocone tilt). The former arrangement showed no change for Ar signals but, instead, revealed ×3 higher signals for Ca, Zn, Mn and Cu and ×7 higher signals for Si and the elements originating from the SS co-sputtering target (Fe, Cr and Ni). Our interpretation of this behavior of X-ray fluorescence signal is that Fe, Cr, Ni and Si most likely originate from the same analytical volume, which is probed by the X-ray beam with far from grazing incidence angle. This is why their signal intensities cannot be used for quantification based on calibration curves constructed for grazing incidence. On the other hand, Ca, Zn, Mn and Cu apparently come from a different analytical volume, such as the surface of the sample, which they may have contaminated after the ion irradiation experiments on one of multiple sample characterization steps.

To summarize the results of our TXRF characterization, the formation of the nanocone arrays appears to be assisted by the sputter co-deposited metal impurity atoms that become recoil-mixed into the near-surface layer of Si in the process of ion irradiation. Moreover, there seems to be some threshold concentration of such atoms which triggers the formation of nanocones (i.e. the cone popping-up process observed in Figs. 3b and 4a). For example, the diffusion of ion-mixed metal atoms towards the surface in conjunction with the diffusion of not yet ion-mixed co-deposited metal atoms over the surface could lead to a nucleation of metal clusters that locally change the sputter erosion rate and thus seed nanocone formation. Similar mechanisms were previously proposed for other ion irradiation induced nanopatterns [9, 10]. However, testing this hypothesis is not trivial and requires carefully planned future experiments.

On the other hand, our TXRF measurements provided an important information about the state of the very thin layer immediately under ion irradiated surface. The estimate of the thickness of this layer (from SRIM-2013 simulations [77]) shows for 75° incidence of 1 keV Ar^+ ions on Si an ion range of just 1.6 nm (with the "tail" of ion distribution ending at about 6 nm). In fact, these values for ion ranges in our irradiation conditions are only about ×10 larger than the native surface roughness of Si wafers. The probing depth of TXRF (reported to be 3-10 nm [63-65]) matches well to the thickness of this amorphous layer, which helps reveal that it contains Ar and metal impurity atoms. This experimental observation agrees with conclusions

of other works obtained using other (often indirect) experimental techniques [9]. Moreover, TXRF allows us to semi-quantitatively estimate concentrations of these impurities under our irradiation conditions to be in a few percent range. Note that in contrast to typical ion implanted crystalline solids, these impurities are not interstitial defects in the lattice (because there are no interstitials in amorphous materials). The state of this near-surface material can be called an *amorphous solid solution* of Si with significant concentrations of Ar and metal impurities.

The concept of silicide induced ion beam patterning of Si [40] emerged as a very popular topic discussed in the literature in recent years [25, 41-43, 61, 78, 79], and it is not surprising that theoretical models have been developed that predict a major role of the metal silicides in the pattern formation [5, 32, 80]. Fundamentally, this concept is based on formation of chemical bonds in the described above layer of material where Si is mixed with metal impurity atoms. When one looks in this literature for experimental evidence of metal silicide formation under ion irradiation, it becomes obvious that the vast majority of data is obtained by XPS and occasionally supported by X-ray absorption near edge spectroscopy (XANES) [41, 79].

We also employed the XPS technique to characterize our samples with nanocone arrays fabricated with the assistance of metal impurity deposition. Aiming to clarify whether the formation of iron, chrome or nickel silicides on the surface had any influence in growth of the nanocone arrays on it, we compared XPS spectra acquired on surface spots located between regions A and B of the sample (as shown in Fig. 3h, with surface morphology on spot A approximately corresponding to Fig. 3a, and on spot B to Fig. 3f). The location of these regions (in the direction from A to C across the sample) approximately corresponds to where TXRF measurements were conducted, with a difference that the analytical spot size of XPS (determined by the focal point of the energy analyzer) was <1 mm in diameter. The results of these measurements are shown in Fig. 8 and summarized in Table 2. Fig. 8 shows 2p XPS peaks for Si, Fe, Cr and Ni, with region B on the bottom and region A on the top. The analysis of the main peak positions reveals only minor shifts towards higher binding energy between regions A and B: the same +0.09 eV for Si, Fe and Ni, and slightly larger shifts of +0.19 eV for Cr. The observation of such minor shifts and, especially, the same shift values for different elements suggest that we saw no difference in chemical bonding between regions A and B – in terms of silicide formation. The representation of the near-surface region after ion irradiation

of Si as a thin amorphous layer with mixed Si and metal impurity atoms has been long accepted in the literature [9, 10, 40, 61, 62]. Probing this layer with the XPS technique in order to detect minor shifts in peak positions and interpret them as indication of formation of new chemical bonds, especially metal silicides, requires careful consideration of possible artifacts because the energy of photoelectrons detected in XPS depends of their escape process, which, in turn, depends on many factors such as material crystallinity, surface morphology and composition. In our experiments, it is much more likely that the observed binding energy shifts result from the local change of effective surface work function due to the change in surface morphology (see Fig. 3) and/or composition (see Table 2). We do not know whether the silicides had formed in both regions at some earlier moments corresponding to lower ion fluences when the nanorippled structure was forming. But regardless of whether or not silicides were present in either region), we conclude that our measurements indicate it is unlikely that the formation of iron, chrome or nickel silicides explains the difference in surface structure, namely its transition from nanorippled morphology (Fig. 3a) to nanocone arrays (Figs. 3c,d and e).

By integrating the XPS peaks, we estimated atomic concentrations of main elements in this sample. The Table 2 lists them for Si, O, C, Fe, Cr, Ni and Ar. For Fe, Cr and Ni concentrations, the trend is similar to that determined by TXRF: (1) a factor of 5 to 10 difference between regions A and B, with the region A being enhanced in metals, (2) a concentration of Fe in region A on the order of a few atomic percent. Thus both XPS and TXRF confirm that the region covered by nanocone arrays (A) contains noticeably more metal impurity atoms than the one covered by nascent nanoripples (B).

Interestingly, our XPS measurements revealed one more difference between regions A and B. For Si, Fe and, particularly, Cr, the ratios between the main elemental peak and its satellites corresponding to different oxidation states changes while going from nanorippled to nanocone array covered region. Namely, the side peaks grow while main peaks become smaller. This suggests an enhancement of oxide formation on the region with nanocones. For example, for Cr we observed that selected oxidation states can become enhanced compared to others (See Fig. 8a and compare spectra for position between A and B with position A). Note, that these observations are made for XPS peaks of the corresponding metals and not for those of oxygen – because silicon oxide was a dominant contributor there. It is possible that oxide molecules

sputtered from the chromium oxide layer on SS surfaces (typical thickness from 0.5 nm to a few nm [81]) could be re-deposited on the Si surface at initial stages of ion irradiation. But the metal oxides we talking about here were detected after completion of the irradiation. Ion fluences greater than 3×10^{18} ions/cm^2, at which we observe nanocones, bring more than 2000 Ar^+ ions per each Si atom on the surface. Even if sputtering yields of Si and SS at grazing incidence angle are not very high, it is highly likely that few nm thin native oxide layers will be sputtered away from both surfaces at such high ion fluences. This is why we assume that the oxides detected with XPS formed after the end of ion irradiation when samples are taken out of the vacuum chamber. At this point, we can hypothesize that the fabrication of nanocone arrays on the surface may result in higher chemical reactivity.

4. Conclusions

We have demonstrated that large nanocone arrays can be fabricated on Si surfaces by grazing incidence irradiation with 1 keV Ar^+ ions concurrently sputtering the surface and depositing metal impurity atoms on it. We compared three materials as co-sputtering targets: Si, Cu and stainless steel and found that only using the steel resulted in growth of dense arrays of nanocones at ion fluences between 10^{18} and 10^{19} ions/cm^2. Our structural characterization of the samples with SEM and AFM techniques revealed that, at these ion fluences, regions far away from co-sputtering targets are covered with nanoripples, and that nanocones popped-up out of the rippled surfaces when moving closer to co-sputtering targets, with their density gradually increasing and reaching saturation in the regions close to these targets. Our characterization of the samples' chemical composition with TXRF and XPS techniques revealed that the concentration of metal impurities originating from stainless steel (Fe, Cr and Ni) was relatively high in the regions with high density of nanocones (Fe reaching a few atomic percent) and much lower (factor of 10 or lower) in the region of nanoripples. TXRF measurements showed that higher concentrations of these impurities are accumulated under the surface in both regions. XPS experiments showed no direct evidence of metal silicide formation occurring on one region only (nanocones or nanoripples) and thus showed that this process could not be the driver of nanocone array formation. Also, XPS measurements revealed enhancement in oxide formation on regions covered by nanocones. Overall, our results suggest that the difference in concentration of metal impurities in the thin near-surface layer forming

under ion irradiation might be responsible for the differences in surface structures. However, we hypothesize that this happens not via formation of new chemical bonds between Si and metals but rather via nucleation of metal seeds when concentration of surface impurity atoms increases over a certain threshold.

Acknowledgements

This work was supported by the U.S. National Science Foundation (DMR-1206175) and the University of Illinois at Chicago. The authors would like to thank to thank Ms. Olivia Thomson and Dr. Seyoung An for their help with sample characterization and for technical training in using SEM and AFM, respectively.

References

[1] U. Valbusa, C. Boragno, F.B. De Mongeot, Nanostructuring surfaces by ion sputtering, Journal of Physics: Condensed Matter, 14 (2002) 8153-8175.
[2] H. Hofsäss, K. Zhang, Surfactant sputtering, Applied Physics A, 92 (2008) 517-524.
[3] H. Hofsäss, K. Zhang, Fundamentals of surfactant sputtering, Nuclear Instruments and Methods in Physics Research Section B: Beam Interactions with Materials and Atoms, 267 (2009) 2731-2734.
[4] F. Frost, B. Ziberi, A. Schindler, B. Rauschenbach, Surface engineering with ion beams: from self-organized nanostructures to ultra-smooth surfaces, Applied Physics A, 91 (2008) 551-559.
[5] K. Zhang, M. Brötzmann, H. Hofsäss, Surfactant-driven self-organized surface patterns by ion beam erosion, New Journal of Physics, 13 (2011) 013033.
[6] S. Macko, F. Frost, M. Engler, D. Hirsch, T. Höche, J. Grenzer, T. Michely, Phenomenology of iron-assisted ion beam pattern formation on Si(001), New Journal of Physics, 13 (2011) 073017.
[7] G. Ozaydin-Ince, K.F. Ludwig Jr, In situ x-ray studies of native and Mo-seeded surface nanostructuring during ion bombardment of Si (100), Journal of Physics: Condensed Matter, 21 (2009) 224008.
[8] A. Keller, S. Facsko, Ion-Induced Nanoscale Ripple Patterns on Si Surfaces: Theory and Experiment, Materials, 3 (2010) 4811-4841.
[9] J. Muñoz-García, L. Vázquez, M. Castro, R. Gago, A. Redondo-Cubero, A. Moreno-Barrado, R. Cuerno, Self-organized nanopatterning of silicon surfaces by ion beam sputtering, Materials Science and Engineering: R: Reports, 86 (2014) 1-44.
[10] J. Muñoz-García, L. Vázquez, R. Cuerno, J.A. Sánchez-García, M. Castro, R. Gago, Self-organized surface nanopatterning by ion beam sputtering, in: Toward Functional Nanomaterials, Springer, 2009, pp. 323-398.
[11] M. Cornejo, B. Ziberi, C. Meinecke, D. Hirsch, J.W. Gerlach, T. Höche, F. Frost, B. Rauschenbach, Self-organized patterning on Si(001) by ion sputtering with simultaneous metal incorporation, Applied Physics A, 102 (2011) 593-599.
[12] R. Cunningham, P. Haymann, C. Lecomte, W. Moore, J. Trillat, Etching of Surfaces with 8‐Kev Argon Ions, Journal of applied physics, 31 (1960) 839-842.
[13] M. Navez, D. Chaperot, C. Sella, Microscopie electronique—etude de lattaque du verre par bombardement ionique, CR Hebd. Seances Acad. Sci, 254 (1962) 240.
[14] W.L. Chan, E. Chason, Making waves: Kinetic processes controlling surface evolution during low energy ion sputtering, Journal of applied physics, 101 (2007) 121301-121301-121346.
[15] T. Luttrell, M. Batzill, Nanoripple formation on TiO_2 (110) by low-energy grazing incidence ion sputtering, Physical Review B, 82 (2010) 035408.
[16] S. Facsko, T. Dekorsy, C. Koerdt, C. Trappe, H. Kurz, A. Vogt, H.L. Hartnagel, Formation of ordered nanoscale semiconductor dots by ion sputtering, Science, 285 (1999) 1551-1553.
[17] J. Zhou, M. Hildebrandt, M. Lu, Self-organized antireflecting nano-cone arrays on Si (100) induced by ion bombardment, Journal of Applied Physics, 109 (2011) 053513.

[18] T.W. Oates, A. Keller, S. Facsko, A. Mücklich, Aligned silver nanoparticles on rippled silicon templates exhibiting anisotropic plasmon absorption, Plasmonics, 2 (2007) 47-50.
[19] S. Camelio, D. Babonneau, D. Lantiat, L. Simonot, F. Pailloux, Anisotropic optical properties of silver nanoparticle arrays on rippled dielectric surfaces produced by low-energy ion erosion, Physical Review B, 80 (2009) 155434.
[20] T. Oates, A. Keller, S. Noda, S. Facsko, Self-organized metallic nanoparticle and nanowire arrays from ion-sputtered silicon templates, Applied physics letters, 93 (2008) 063106-063106-063103.
[21] A. Toma, D. Chiappe, C. Boragno, F.B. de Mongeot, Self-organized ion-beam synthesis of nanowires with broadband plasmonic functionality, Physical Review B, 81 (2010) 165436.
[22] F. Frost, B. Ziberi, T. Höche, B. Rauschenbach, The shape and ordering of self-organized nanostructures by ion sputtering, Nuclear Instruments and Methods in Physics Research Section B: Beam Interactions with Materials and Atoms, 216 (2004) 9-19.
[23] M. Cornejo, J. Völlner, B. Ziberi, F. Frost, B. Rauschenbach, Ion Beam Sputtering: A Route for Fabrication of Highly Ordered Nanopatterns, in: Fabrication and Characterization in the Micro-Nano Range, Springer, 2011, pp. 69-94.
[24] M. Castro, R. Cuerno, L. Vázquez, R. Gago, Self-organized ordering of nanostructures produced by ion-beam sputtering, Physical review letters, 94 (2005) 016102.
[25] R. Gago, A. Redondo-Cubero, F.J. Palomares, L. Vazquez, Influence of metal co-deposition on silicon nanodot patterning dynamics during ion-beam sputtering, Nanotechnology, 25 (2014) 415301.
[26] Q. Li, Z. Ni, S. Yang, J. Gong, D. Zhu, Z. Zhu, Large-area and high-density silicon nanocone arrays by Ar+ sputtering at room temperature, Nuclear Instruments and Methods in Physics Research Section B: Beam Interactions with Materials and Atoms, 266 (2008) 197-202.
[27] S. Macko, F. Frost, B. Ziberi, D.F. Forster, T. Michely, Is keV ion-induced pattern formation on Si(001) caused by metal impurities?, Nanotechnology, 21 (2010) 85301.
[28] S. Macko, J. Grenzer, F. Frost, M. Engler, D. Hirsch, M. Fritzsche, A. Mücklich, T. Michely, Iron-assisted ion beam patterning of Si(001) in the crystalline regime, New Journal of Physics, 14 (2012) 073003.
[29] R.M. Bradley, J.M. Harper, Theory of ripple topography induced by ion bombardment, Journal of Vacuum Science & Technology A: Vacuum, Surfaces, and Films, 6 (1988) 2390-2395.
[30] M.A. Makeev, R. Cuerno, A.-L. Barabási, Morphology of ion-sputtered surfaces, Nuclear Instruments and Methods in Physics Research Section B: Beam Interactions with Materials and Atoms, 197 (2002) 185-227.
[31] R. Cuerno, M. Castro, J. Muñoz-García, R. Gago, L. Vázquez, Nanoscale pattern formation at surfaces under ion-beam sputtering: A perspective from continuum models, Nuclear Instruments and Methods in Physics Research Section B: Beam Interactions with Materials and Atoms, 269 (2011) 894-900.
[32] R.M. Bradley, Theory of nanodot and sputter cone arrays produced by ion sputtering with concurrent deposition of impurities, Physical Review B, 83 (2011).

[33] J. Wadsworth, G. Crabtree, R. Hemley, (chairs), R. Falcone, I. Robertson, J. Stringer, P. Tortorelli, G.T.R. Gray, M. Nicol, J. Lehr, S.W. Tozer, T.D. de la Rubia, T. Fitzsimmons, J.S. Vetrano, Basic Research Needs for Materials under Extreme Environments, in: J. Wadsworth, G. Crabtree, R. Hemley (Eds.) Report of the BES Workshop on Basic Research Needs for Materials under Extreme Environments, June 11-13, 2007, U. S. Department of Energy's Basic Energy Sciences Program, Washington, DC, 2007.
[34] D. Carbone, A. Biermanns, B. Ziberi, F. Frost, O. Plantevin, U. Pietsch, T. Metzger, Ion-induced nanopatterns on semiconductor surfaces investigated by grazing incidence x-ray scattering techniques, Journal of Physics: Condensed Matter, 21 (2009) 224007.
[35] G. Ozaydin, A.S. Özcan, Y. Wang, K.F. Ludwig, H. Zhou, R.L. Headrick, D.P. Siddons, Real-time x-ray studies of Mo-seeded Si nanodot formation during ion bombardment, Applied Physics Letters, 87 (2005) 163104.
[36] J.A. Sanchez-Garcia, L. Vazquez, R. Gago, A. Redondo-Cubero, J.M. Albella, Z. Czigany, Tuning the surface morphology in self-organized ion beam nanopatterning of Si(001) via metal incorporation: from holes to dots, Nanotechnology, 19 (2008) 355306.
[37] G. Ozaydin, K.F. Ludwig, H. Zhou, R.L. Headrick, Effects of Mo seeding on the formation of Si nanodots during low-energy ion bombardment, Journal of Vacuum Science & Technology B: Microelectronics and Nanometer Structures, 26 (2008) 551.
[38] K. Zhang, O. Bobes, H. Hofsass, Designing self-organized nanopatterns on Si by ion irradiation and metal co-deposition, Nanotechnology, 25 (2014) 085301.
[39] R. Kree, T. Yasseri, A.K. Hartmann, Surfactant Sputtering: Theory of a new method of surface nanostructuring by ion beams, Nuclear Instruments and Methods in Physics Research Section B: Beam Interactions with Materials and Atoms, 267 (2009) 1403-1406.
[40] M. Engler, F. Frost, S. Muller, S. Macko, M. Will, R. Feder, D. Spemann, R. Hubner, S. Facsko, T. Michely, Silicide induced ion beam patterning of Si(001), Nanotechnology, 25 (2014) 115303.
[41] B. Khanbabaee, D. Lützenkirchen-Hecht, R. Hübner, J. Grenzer, S. Facsko, U. Pietsch, Near surface silicide formation after off-normal Fe-implantation of Si(001) surfaces, Journal of Applied Physics, 116 (2014) 024301.
[42] K. Zhang, H. Hofsäss, H. Zutz, Nanoscale metal-silicide films prepared by surfactant sputtering and analyzed by RBS, Nuclear Instruments and Methods in Physics Research Section B: Beam Interactions with Materials and Atoms, 268 (2010) 1967-1971.
[43] K. Zhang, M. Brötzmann, H. Hofsäss, Sharp transition from ripple patterns to a flat surface for ion beam erosion of Si with simultaneous co-deposition of iron, AIP Advances, 2 (2012) 032123.
[44] S. Chattopadhyay, L.-C. Chen, K.-H. Chen, Nanotips: Growth, Model, and Applications, Critical Reviews in Solid State and Materials Sciences, 31 (2006) 15-53.
[45] J. Shieh, S. Ravipati, F.-H. Ko, K. Ostrikov, Plasma-made silicon nanograss and related nanostructures, Journal of Physics D: Applied Physics, 44 (2011) 174010.
[46] Y. Yaakob, Y. Kuwataka, M.Z.M. Yusop, S. Tanaka, M.S. Rosmi, G. Kalita, M. Tanemura, Room-temperature growth of ion-induced Si- and Ge-incorporated carbon nanofibers, Physica Status Solidi (b), 252 (2015) 1345-1349.
[47] J.L. Vossen, J. Cuomo, Glow discharge sputter deposition, in: J.L. Vossen, W. Kern (Eds.) Thin film processes, Academic Press, New York, 1978, pp. 12-73.

[48] G. Wehner, D. Hajicek, Cone formation on metal targets during sputtering, Journal of Applied Physics, 42 (1971) 1145-1149.
[49] J.L. Vossen, Inhibition of chemical sputtering of organics and C by trace amounts of Cu surface contamination, Journal of Applied Physics, 47 (1976) 544-546.
[50] S.M. Rossnagel, R.S. Robinson, The time development of impurity-generated sputter cones on copper, Radiation Effects, 58 (1981) 11-16.
[51] L. Qin-Tao, L. Zhi-Gang, X. Qiao-Ling, G. Jin-Long, Z. De-Zhang, Controlled evolution of silicon nanocone arrays induced by Ar^+ sputtering at room temperature, Chinese Physics Letters, 26 (2009) 056102.
[52] X. Zhao, Q. Li, Q. Shi, S. Xue, Z. Li, Y. Liu, Effect of incident angles on the morphology of silicon nanocone array induced by Ar+ sputtering at room temperature, Micro & Nano Letters, 7 (2012) 596.
[53] I. Levchenko, S.Y. Huang, K. Ostrikov, S. Xu, Silicon on silicon: self-organized nanotip arrays formed in reactive Ar+H2 plasmas, Nanotechnology, 21 (2010) 025605.
[54] K. Ostrikov, U. Cvelbar, A.B. Murphy, Plasma nanoscience: setting directions, tackling grand challenges, Journal of Physics D: Applied Physics, 44 (2011) 174001.
[55] Q. Wang, C.Z. Gu, Z. Xu, J.J. Li, Z.L. Wang, X.D. Bai, Z. Cui, Diamond cone arrays with controlled morphologies formed by self-organized selective ions sputtering, Journal of Applied Physics, 100 (2006) 034312.
[56] D.K. Ball, K. Lenz, M. Fritzsche, G. Varvaro, S. Gunther, P. Krone, D. Makarov, A. Mucklich, S. Facsko, J. Fassbender, M. Albrecht, Magnetic properties of granular CoCrPt:SiO 2 thin films deposited on GaSb nanocones, Nanotechnology, 25 (2014) 085703.
[57] H.R. Kaufman, R.S. Robinson, Ion beam texturing of surfaces, Journal of Vacuum Science & Technology, 16 (1979) 175-178.
[58] Y. Choi, A. Zachary, S. Tepavcevic, C. Wu, L. Hanley, Polyatomicity and kinetic energy effects on surface polymerization by ion-assisted deposition, International Journal of Mass Spectrometry, 241 (2006) 139-147.
[59] I.L. Bolotin, S.H. Tetzler, L. Hanley, XPS and QCM Studies of Hydrocarbon and Fluorocarbon Polymer Films Bombarded by 1-20 keV C_{60} Ions, The Journal of Physical Chemistry C, 111 (2007) 9953-9960.
[60] M.W. Majeski, I.L. Bolotin, L. Hanley, Cluster beam deposition of Cu(2-X)S nanoparticles into organic thin films, ACS Appl Mater Interfaces, 6 (2014) 12901-12908.
[61] O. El-Atwani, S. Gonderman, A. DeMasi, A. Suslova, J. Fowler, M. El-Atwani, K. Ludwig, J. Paul Allain, Nanopatterning of metal-coated silicon surfaces via ion beam irradiation: Real time x-ray studies reveal the effect of silicide bonding, Journal of applied physics, 113 (2013) 124305.
[62] O. El-Atwani, A. Suslova, A. DeMasi, S. Gonderman, J. Fowler, M. El-Atwani, K. Ludwig, J. Paul Allain, Real time x-ray studies during nanostructure formation on silicon via low energy ion beam irradiation using ultrathin iron films, Applied physics letters, 101 (2012) 263104.
[63] R. Klockenkämper, A. Prange, Total-reflection X-ray fluorescence analysis, Spectrochimica Acta-B-Atomic Spectroscopy-including free Diskettes, 52 (1997) 1071.
[64] R. Klockenkämper, A. von Bohlen, Total-Reflection X-Ray Fluorescence Analysis and Related Methods, John Wiley & Sons, 2014.

[65] P. Wobrauschek, Total reflection x‐ray fluorescence analysis—a review, X‐Ray Spectrometry, 36 (2007) 289-300.
[66] M. Teichmann, J. Lorbeer, F. Frost, B. Rauschenbach, Ripple coarsening on ion beam-eroded surfaces, Nanoscale research letters, 9 (2014) 1-8.
[67] T. Basu, D.P. Datta, T. Som, Transition from ripples to faceted structures under low-energy argon ion bombardment of silicon: understanding the role of shadowing and sputtering, Nanoscale research letters, 8 (2013) 1-8.
[68] T. Basu, T. Som, Temporal evolution of ripple pattern on silicon surface: An ion induced solid flow approach, Applied Surface Science, 310 (2014) 142-146.
[69] T. Basu, J.R. Mohanty, T. Som, Unusual pattern formation on Si(1 0 0) due to low energy ion bombardment, Applied Surface Science, 258 (2012) 9944-9948.
[70] Y. Lifshitz, S. Kasi, J. Rabalais, Subplantation model for film growth from hyperthermal species: Application to diamond, Physical review letters, 62 (1989) 1290.
[71] Y. Lifshitz, S. Kasi, J. Rabalais, W. Eckstein, Subplantation model for film growth from hyperthermal species, Physical Review B, 41 (1990) 10468.
[72] P. Sigmund, A. Gras-Marti, Theoretical aspects of atomic mixing by ion beams, Nuclear Instruments and Methods, 182 (1981) 25-41.
[73] A. Barcz, B. Paine, M.A. Nicolet, Ion mixing of markers in SiO2 and Si, Applied Physics Letters, 44 (1984) 45-47.
[74] A. Hamdi, M.-A. Nicolet, Cobalt silicide formation by ion mixing, Thin Solid Films, 119 (1984) 357-364.
[75] S. Ulrich, J. Schwan, W. Donner, H. Ehrhardt, Knock-on subplantation-induced formation of nanocrystalline c-BN with r.f. magnetron sputtering and r.f. argon ion plating, Diamond and Related Materials, 5 (1996) 548-551.
[76] J. Schwan, S. Ulrich, H. Roth, H. Ehrhardt, S.R.P. Silva, J. Robertson, R. Samlenski, R. Brenn, Tetrahedral amorphous carbon films prepared by magnetron sputtering and dc ion plating, Journal of Applied Physics, 79 (1996) 1416-1422.
[77] J.F. Ziegler, M.D. Ziegler, J.P. Biersack, SRIM–The stopping and range of ions in matter (2010), Nuclear Instruments and Methods in Physics Research Section B: Beam Interactions with Materials and Atoms, 268 (2010) 1818-1823.
[78] A. Redondo-Cubero, R. Gago, F.J. Palomares, A. Mücklich, M. Vinnichenko, L. Vázquez, Nanopatterning dynamics on Si(100) during oblique 40-keV Ar^{+} erosion with metal codeposition: Morphological and compositional correlation, Physical Review B, 86 (2012) 085436.
[79] B. Khanbabaee, B. Arezki, A. Biermanns, M. Cornejo, D. Hirsch, D. Lützenkirchen-Hecht, F. Frost, U. Pietsch, Depth profile investigation of the incorporated iron atoms during Kr+ ion beam sputtering on Si (001), Thin Solid Films, 527 (2013) 349-353.
[80] J. Zhou, M. Lu, Mechanism of Fe impurity motivated ion-nanopatterning of Si (100) surfaces, Physical Review B, 82 (2010) 125404.
[81] K. Odaka, S. Ueda, Dependence of outgassing rate on surface oxide layer thickness in type 304 stainless steel before and after surface oxidation in air, Vacuum, 47 (1996) 689-692.

Figure 1.

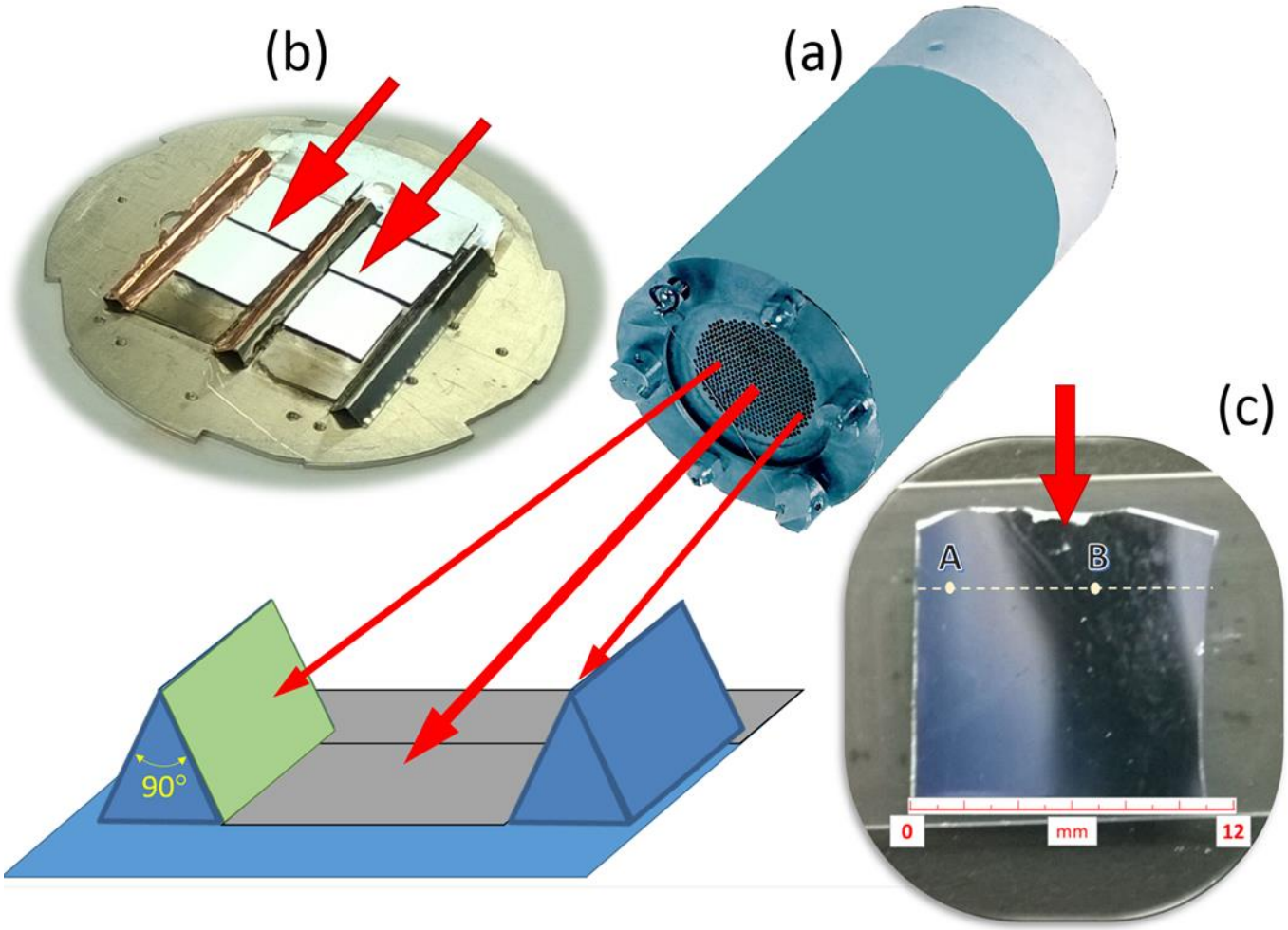

Figure 1.
Schematics of ion irradiation: 3 cm Kaufman-type broad beam ion source is concurrently irradiating the sample plate (Si target shown in grey) and co-sputtering targets (shown in green).
Custom-built sample holder permitting simultaneous irradiation of four samples mounted on Si wafers. Three "ridges" made from bent stainless steel (SS) shim stock were spot welded the sample plate to enable mounting of co-sputtering targets (Cu tape shown here) or serve themselves as such targets. Additional Si wafer pieces were installed on the side where ions are coming from (upper right) in order to prevent deposition of sample plate material on the irradiated samples.
Typical appearance of the ion irradiated sample. Matte regions close to the ridges with co-sputtering targets were confirmed to contain dense arrays of nanocones, while the shiny region in between contained nanoripples. Regions around positions A and B were characterized with different techniques.

Figure 2.

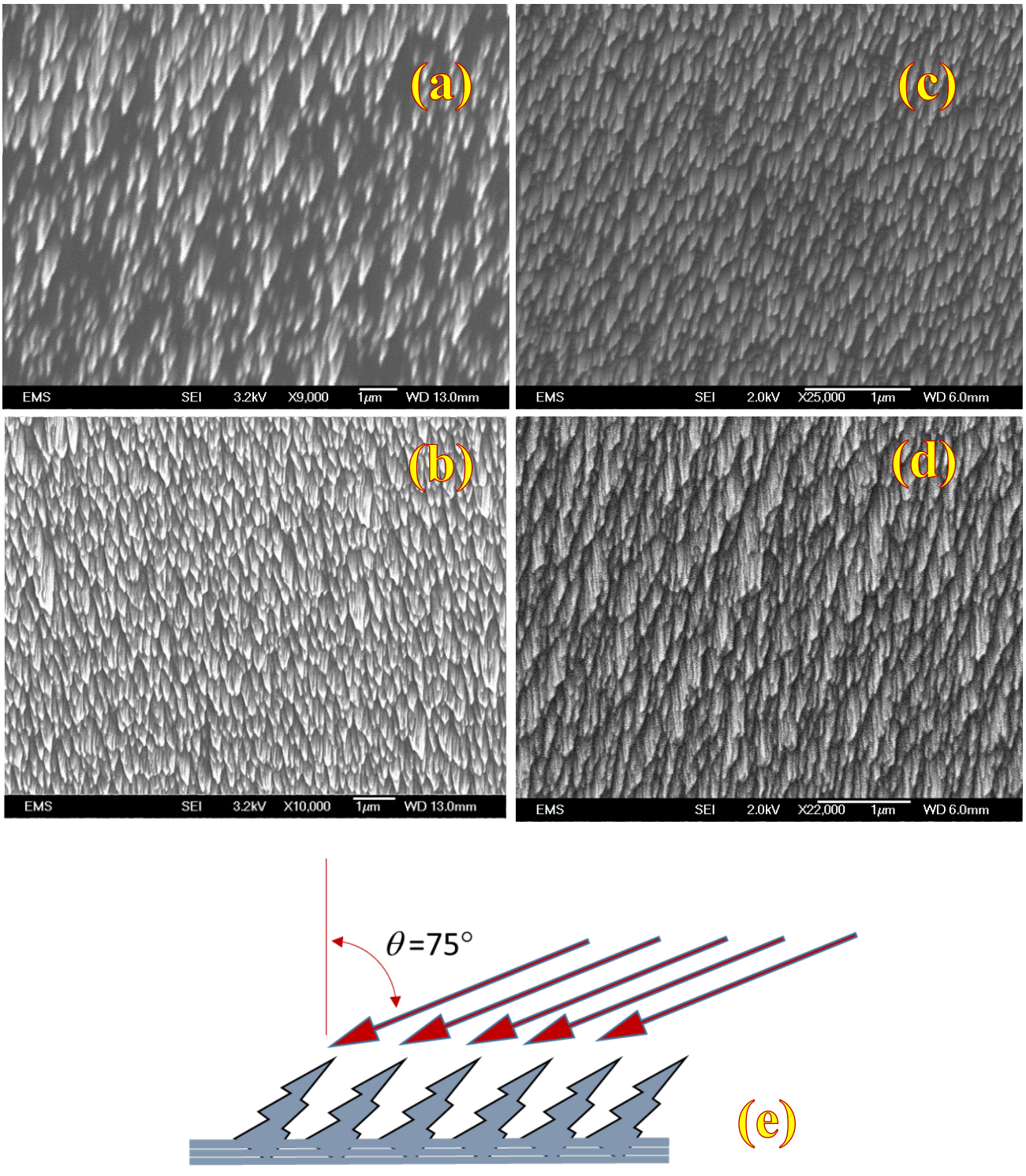
(a)
EMS SEI 3.2kV X9,000 1μm WD 13.0mm
(c)
EMS SEI 2.0kV X25,000 1μm WD 6.0mm
(b)
EMS SEI 3.2kV X10,000 1μm WD 13.0mm
(d)
EMS SEI 2.0kV X22,000 1μm WD 6.0mm
θ=75°
(e)

Figure 2.

Scanning Electron Microscopy images of matte regions on Si samples after irradiation with 1 keV Ar^+ with sputter co-deposition of material from bare SS "ridges" (Fig.1). (a) & (b) and (c) & (d) are grouped according to lateral resolutions.

(a) At irradiation time of 40 minutes (Ar^+ ion fluence ~3×10^{18} ions/cm^2), arrays of nanocones become clearly visible. Individual nanocones reach hundreds of nm in dimensions.

(b) At 80 minutes (~ 6×10^{18} ions/cm^2), the density of nanocones in the array reaches apparent saturation.

(c) and (d) At 100 (~ 7.5×10^{18} ions/cm^2) and 120 minutes (~ 1.2×10^{19} ions/cm^2), a coarsening becomes visible in a saturated array of nanocones, with individual nanocones merging into larger structures.

(e) Schematic depiction of nanocone orientation relative to incident ion beam.

Figures 3a and 3b

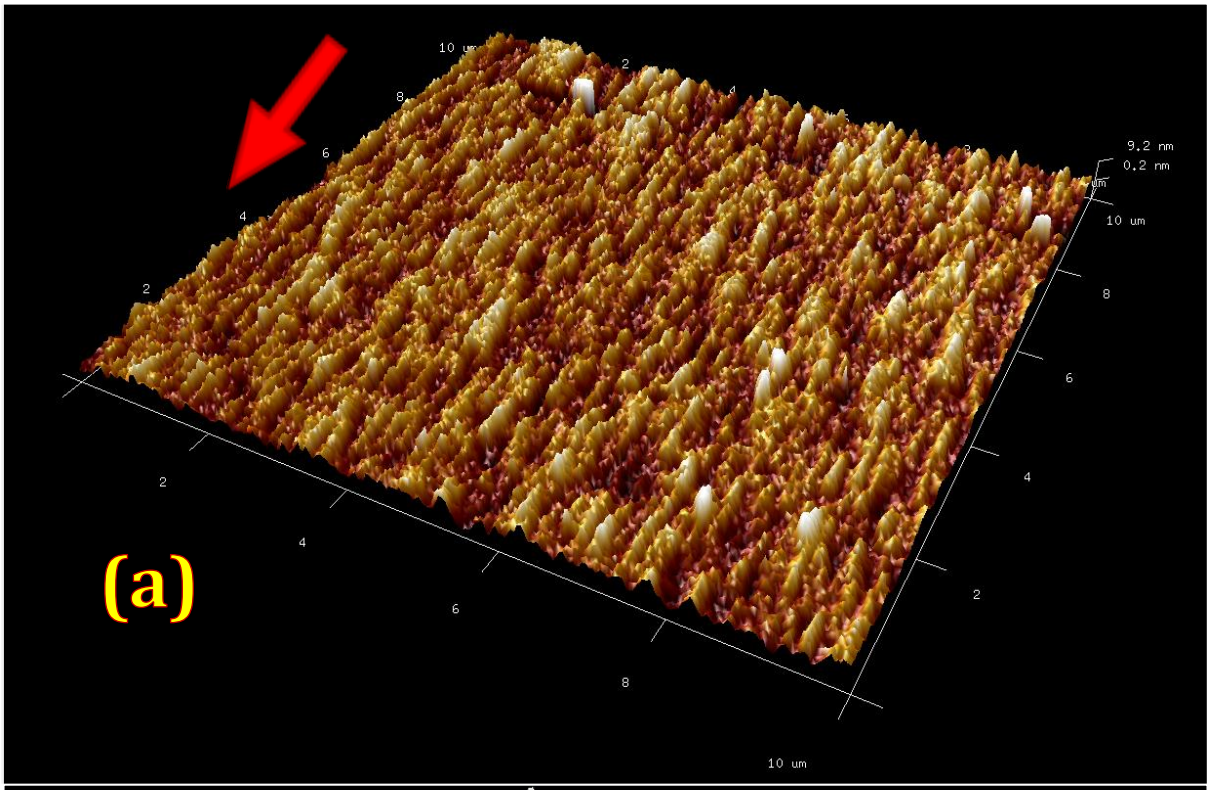

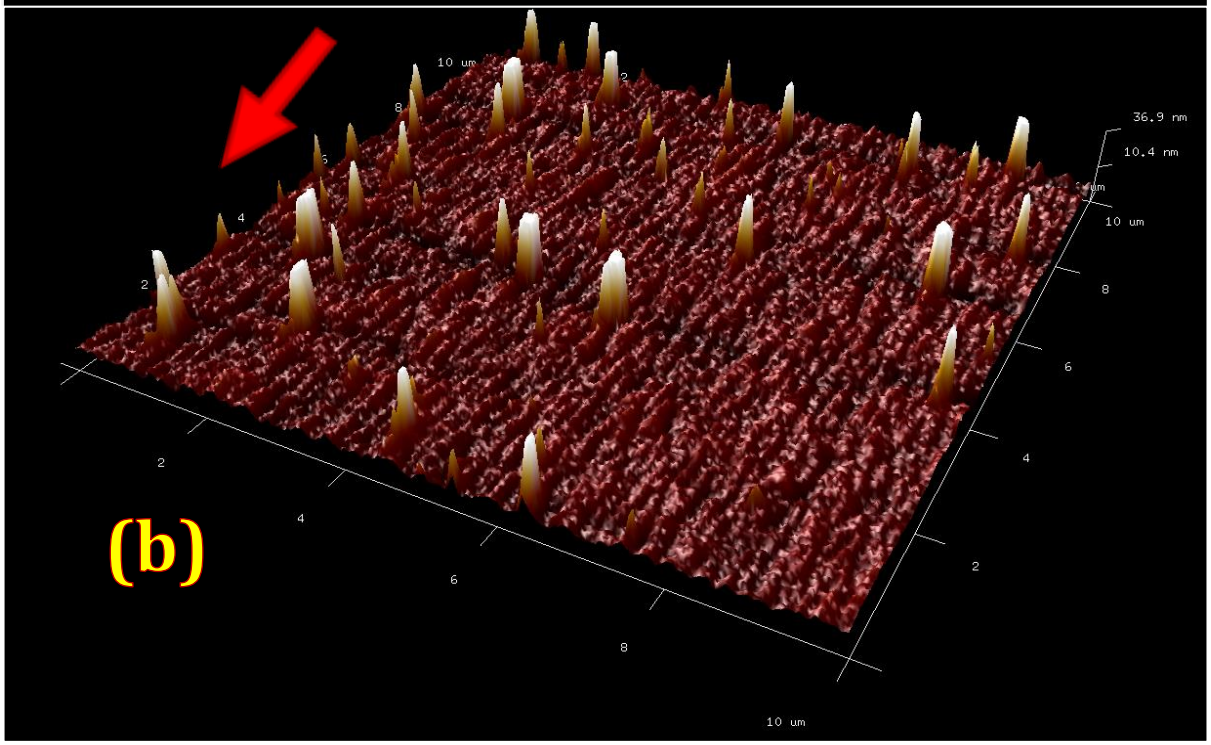

Figures 3c and 3d

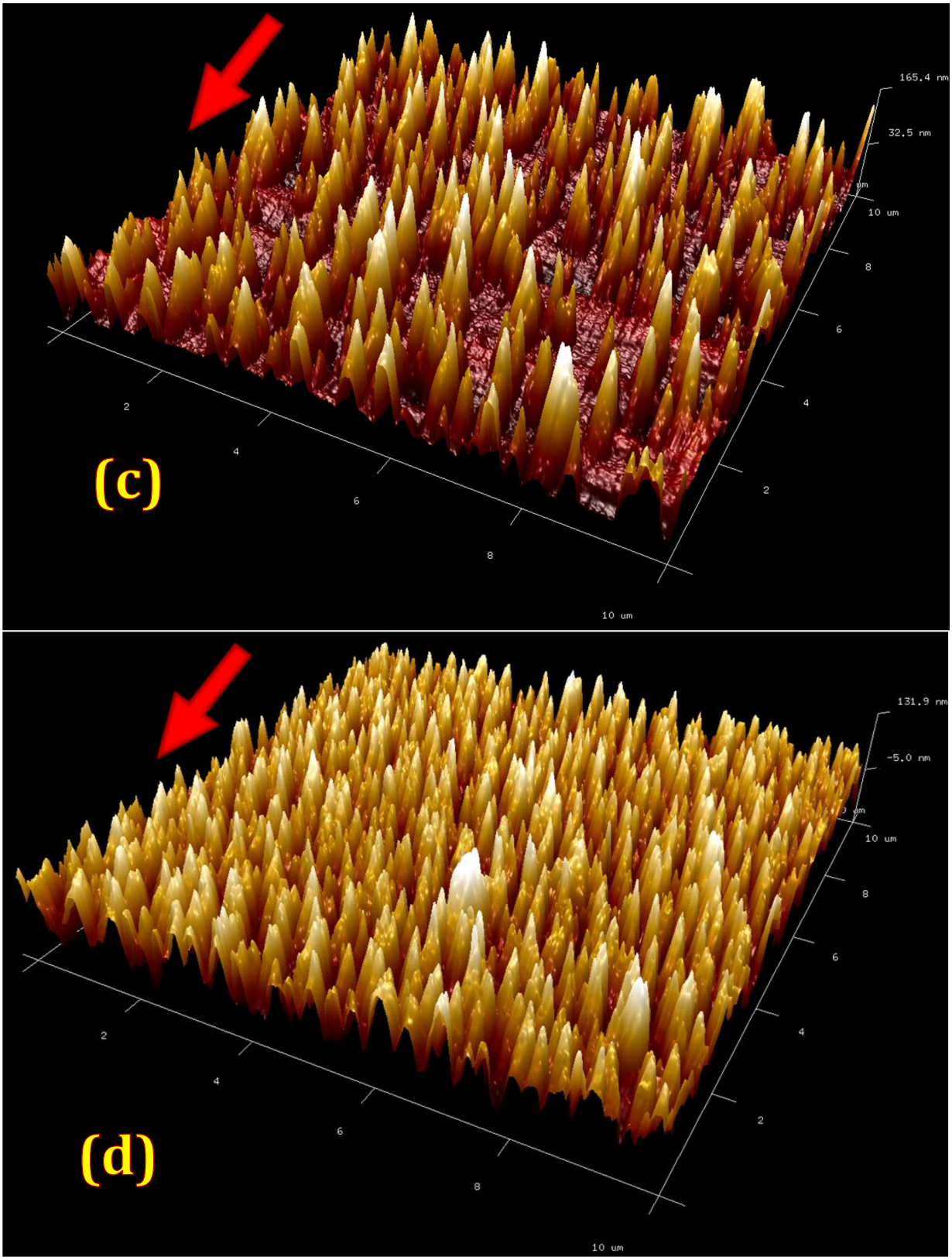

Figure 3e.

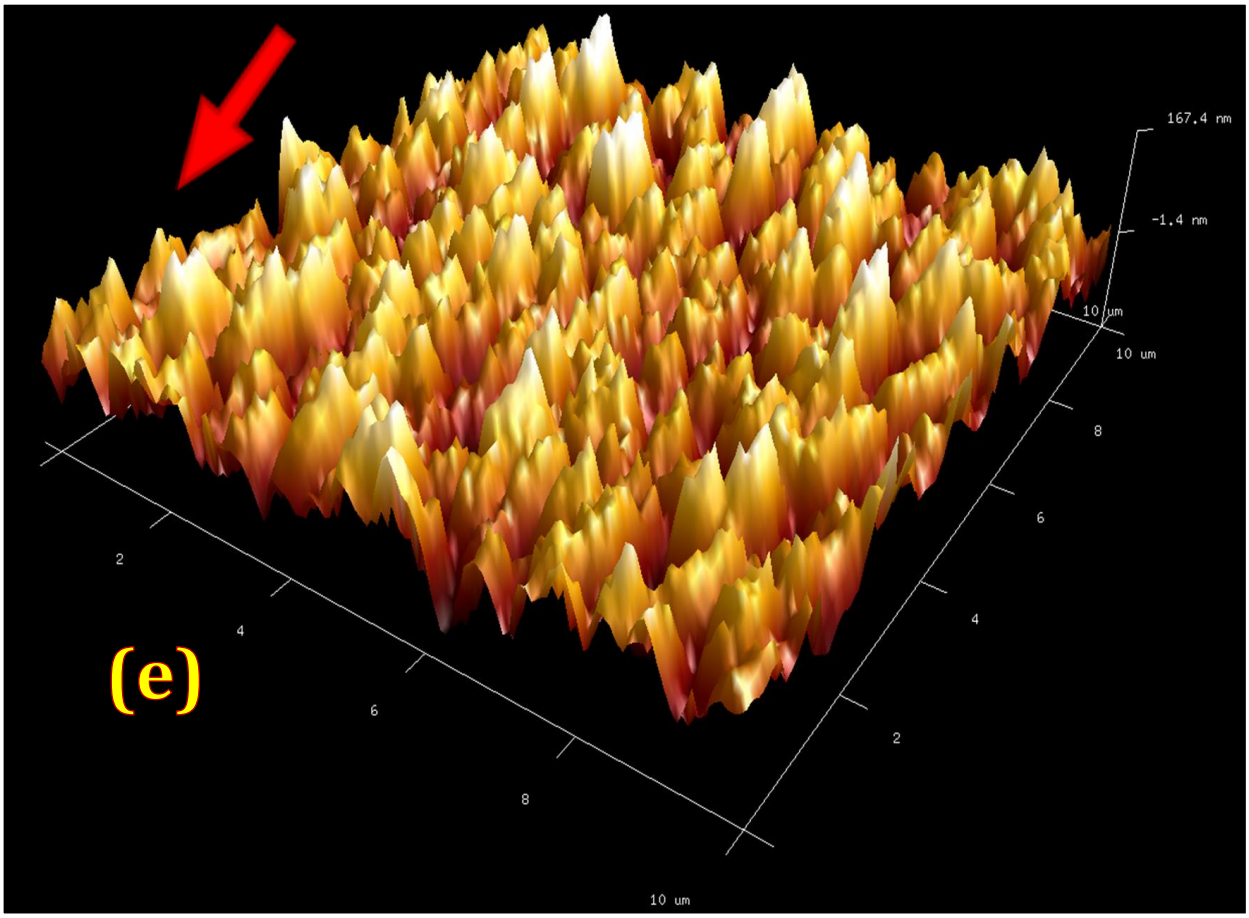

Figure 3

10×10 μm^2 Atomic Force Microscopy images of the Si surface after irradiation with Ar+ ions and co-deposition of atoms from SS sputtering target for the sample shown in Figure 1c. Scans were performed across the sample along the line from A to B (see Fig. 1c).

a) On the shiny region (~6.5 mm from the left edge), no nanocones are seen, only the surface covered with nanoripples oriented along the incidence of the primary ion beam (red arrow)
b) On the transitional area from shiny to matte regions (~6 mm from the left edge), nanocones begin to pop-up out of the nanorippled surface
c) Near the border of the left matte region (~5 mm from the left edge), nanocones are becoming more dense and begin to form arrays.
d) Inside the left matte region (~2 mm from the left edge), nacones have formed a "saturated" in density array.
e) Inside the right matte region (~10 mm from the left edge), the nanocone arrays begin to coarsen, with individual nanocones merging into larger structures, as on Figure 2c and d

Suggested Layout of Figure 3

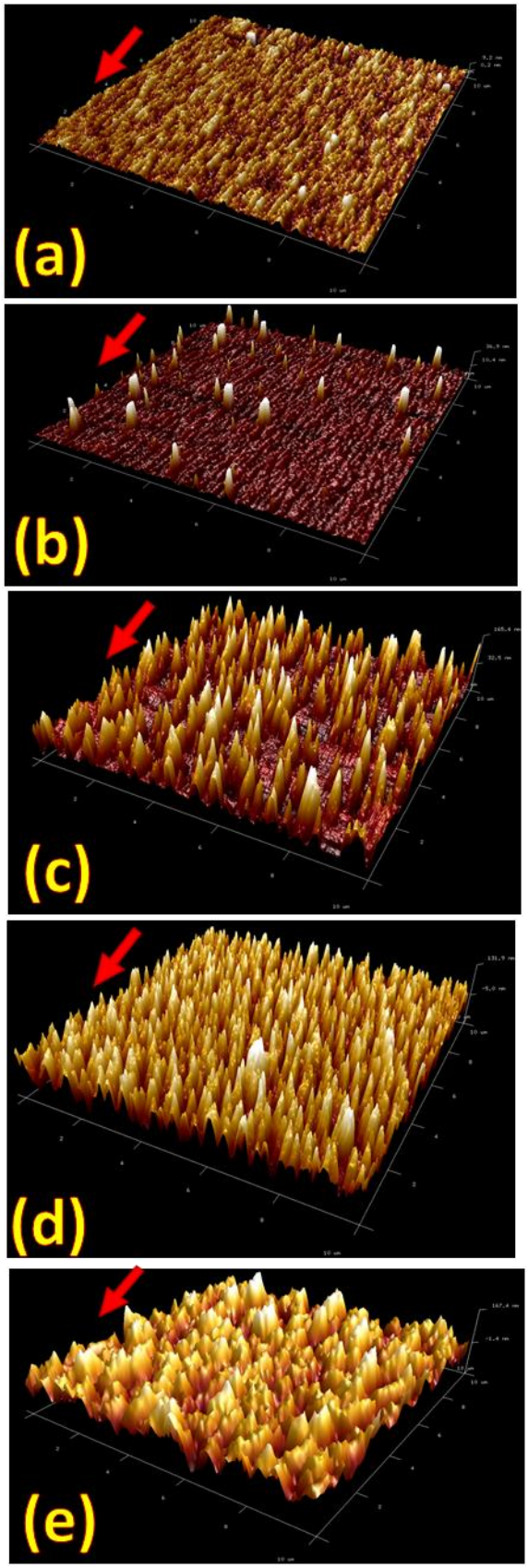

Figure 4.

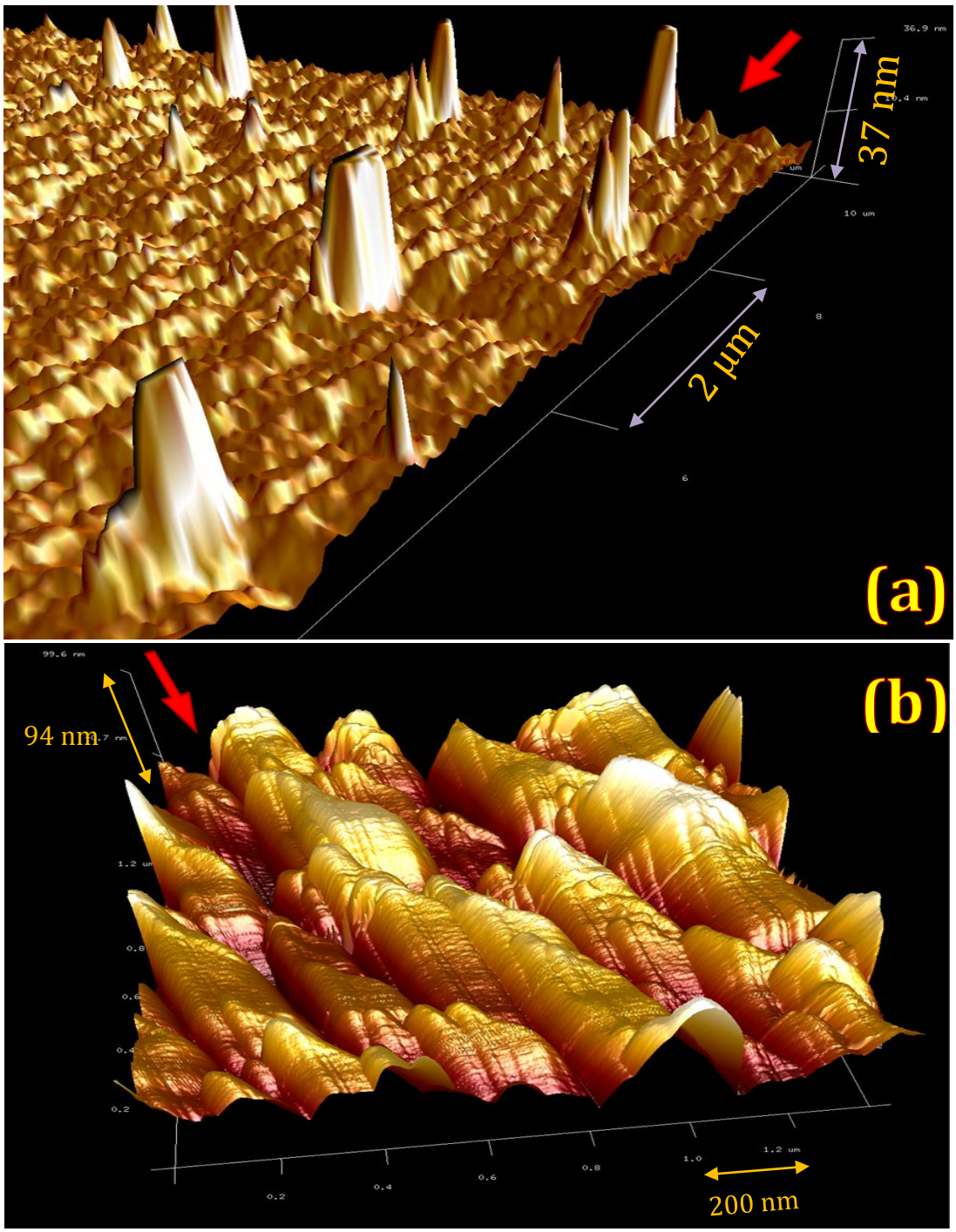

Figure 4.
Closer look at AFM images of matte regions on Si sample from Figure 1c.
(a) Zooming on Figure 3b. The popup formation process of nanocones is apparent.
(b) Higher resolution ($1.4 \times 1.4\ \mu m^2$) imaging of the nanocone in the region around the one on Figure 3d reveals that they have fine grooved / faceted / rippled structure indicating that once the size of nanocones reaches its maximum, its surface begins to self-organize under continuing ion beam irradiation.

Figure 5.

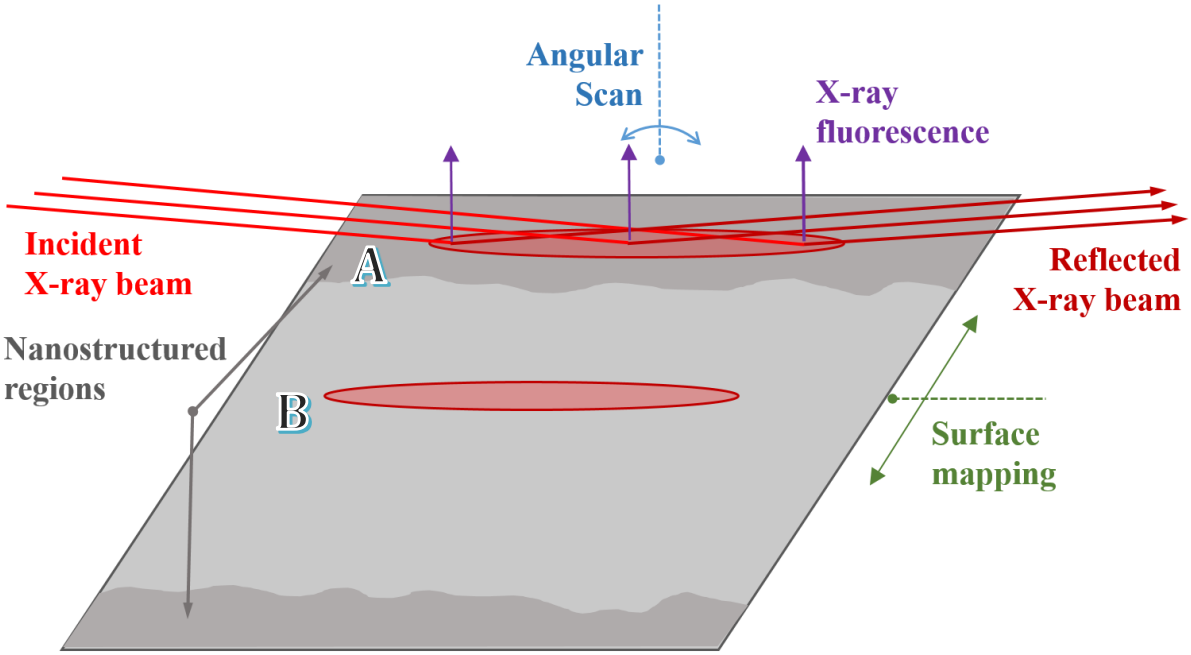

Figure 5.
Schematics of TXRF characterization of the sample from Figure 3. By gradually increasing the incident angle of the primary X-ray beam, its penetration deeper into the bulk and excitation of atoms buried within a few nanometers below the surface can be achieved. Surface mapping is achieved by moving the sample with respect to the X-ray beam, which has a surface footprint of approximately 2 mm × 5 mm. This footprint corresponds to the lateral resolution of this technique.

Figure 6.

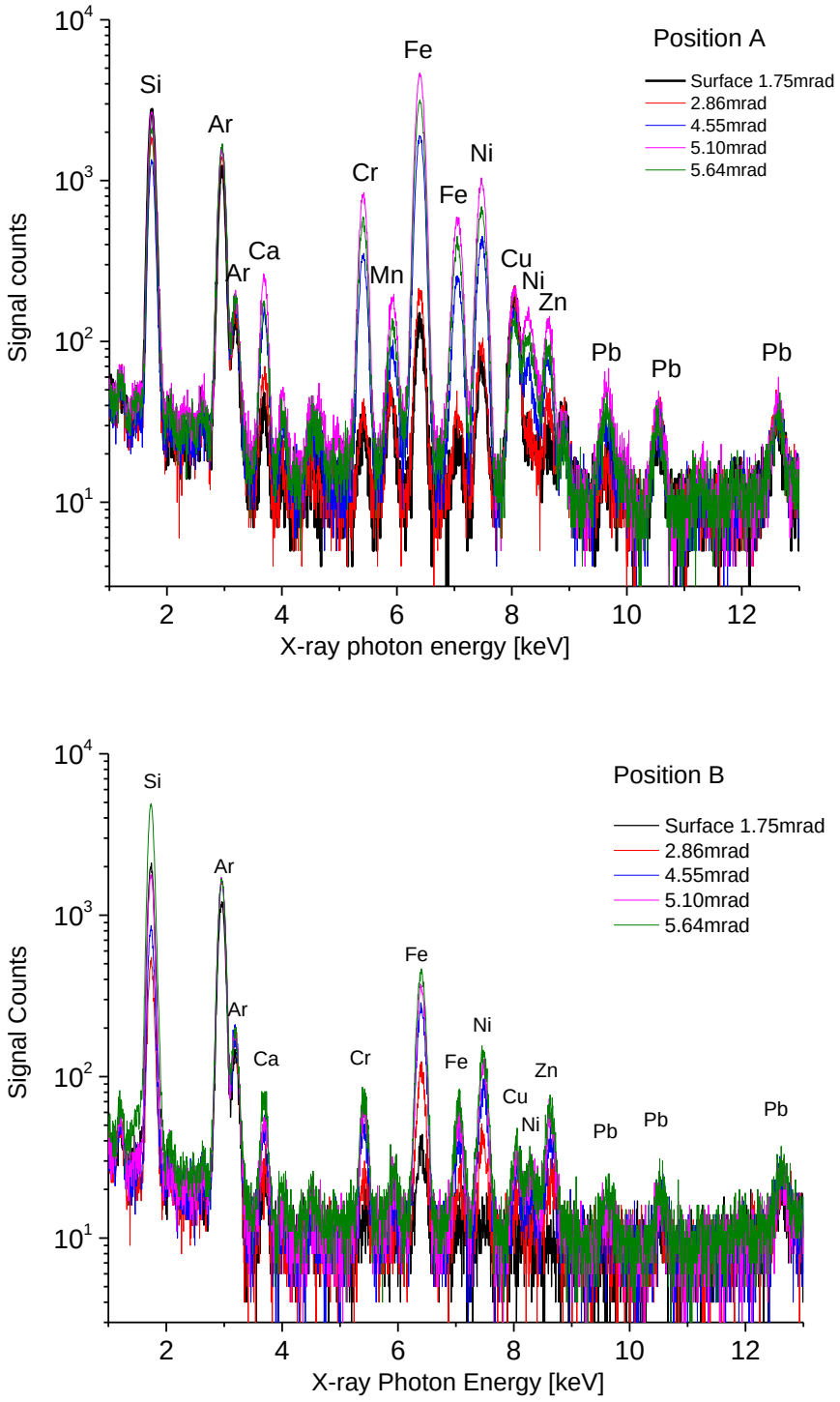
Position A
Surface 1.75mrad
2.86mrad
4.55mrad
5.10mrad
5.64mrad
Signal counts
X-ray photon energy [keV]
Si
Ar
Ca
Ar
Cr
Mn
Fe
Fe
Ni
Cu
Ni
Zn
Pb
Pb
Pb
Position B
Surface 1.75mrad
2.86mrad
4.55mrad
5.10mrad
5.64mrad
Signal Counts
X-ray Photon Energy [keV]
Si
Ar
Ar
Ca
Cr
Fe
Fe
Ni
Cu
Ni
Zn
Pb
Pb
Pb

Figure 6

Results of TXRF measurements at two different locations on the sample from Figure 3, approximately corresponding to Figure 1c, with position A corresponding to a rougher (matte) surface area than position B.

In both cases, angular scans were performed, with the primary X-ray beam angle gradually increasing to penetrate deeper into the bulk of the sample. Signal counting (data acquisition) time was in all cases 2000 seconds. As can be seen, elemental signals for Cr, Mn, Fe, Ni, Cu and Zn increase with increasing incident angle of the primary beam, indicating that these elemental concentrations are higher below the surface than at the surface (black spectrum).

Surface concentrations for the above elements were determined by means of calibration curves measured for each element. These values are summarized in Table 1.

Figure 7.

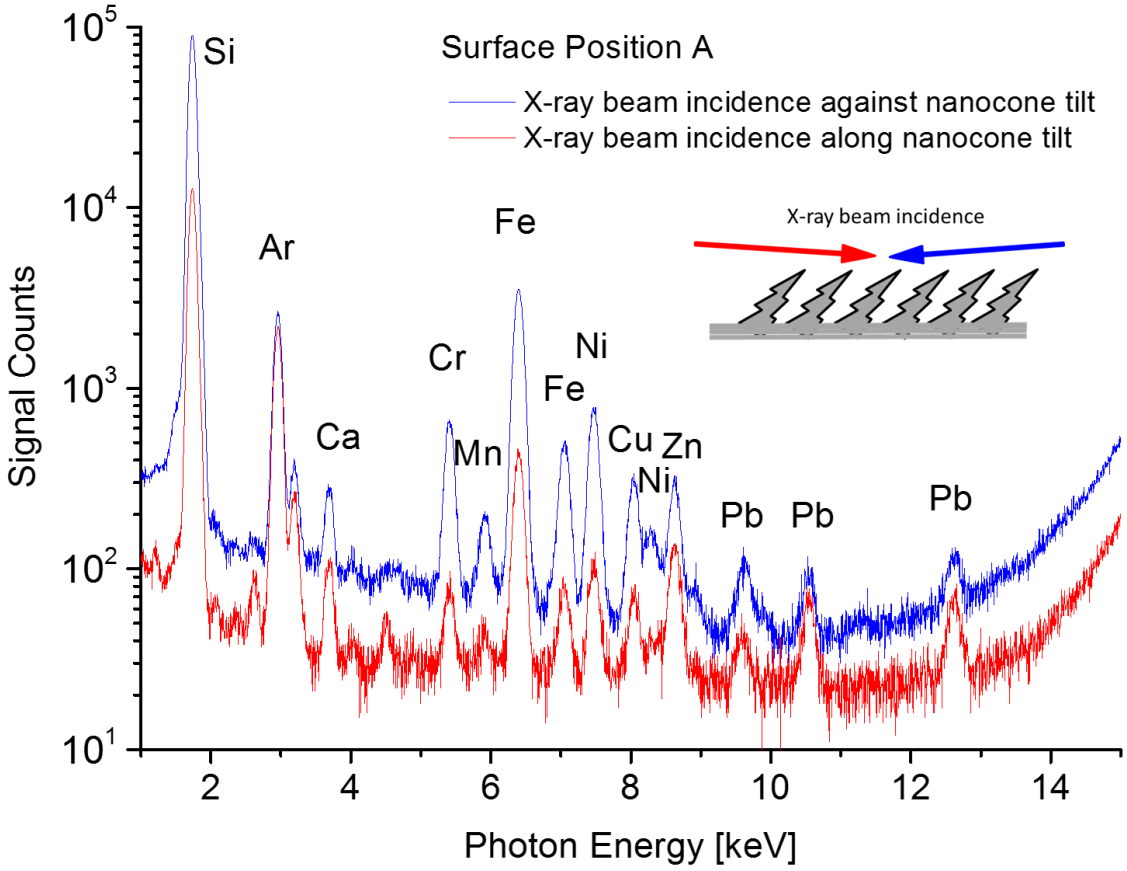

Figure 7
TXRF characterization of the sample from Figure 3 measured on the surface region A (as defined on Figure 1c) with two orientations of the X-ray beam, one coming from the same direction as the ion beam (blue) and the other opposite to it (red). For the former (blue) geometry, ×3 higher signals for Ca, Zn, Mn and Cu and ×7 higher signals for Si and the elements originating from the SS co-sputtering target, Fe, Cr and Ni. This might indicate that Fe, Cr, Ni and Si originate from the same analytical volume, which is probed by the X-ray beam with far from grazing incidence angle, while Ca, Zn, Mn and Cu originate from the other (most likely, the surface).

Figure 8a

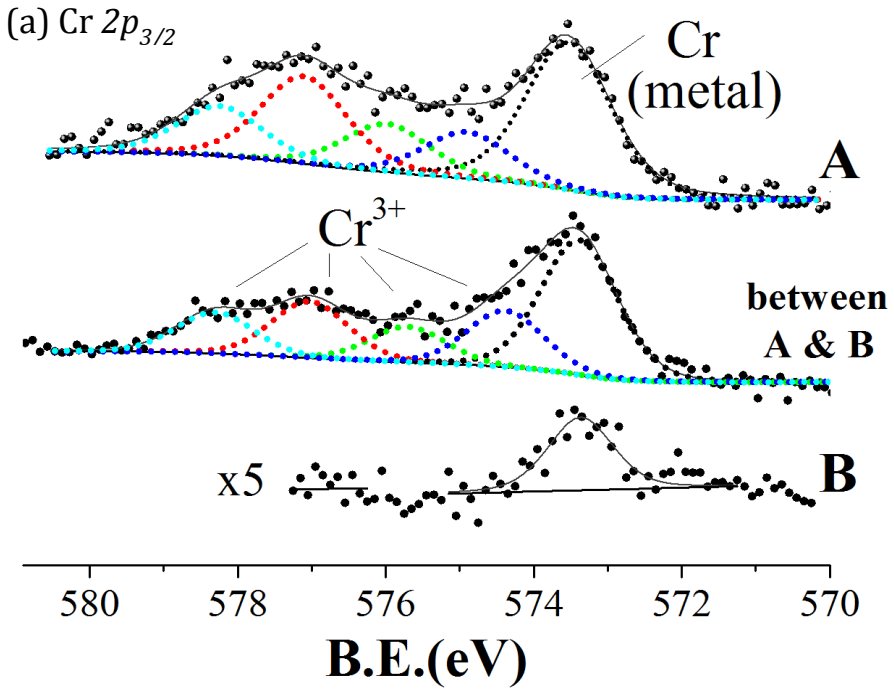

Figure 8b

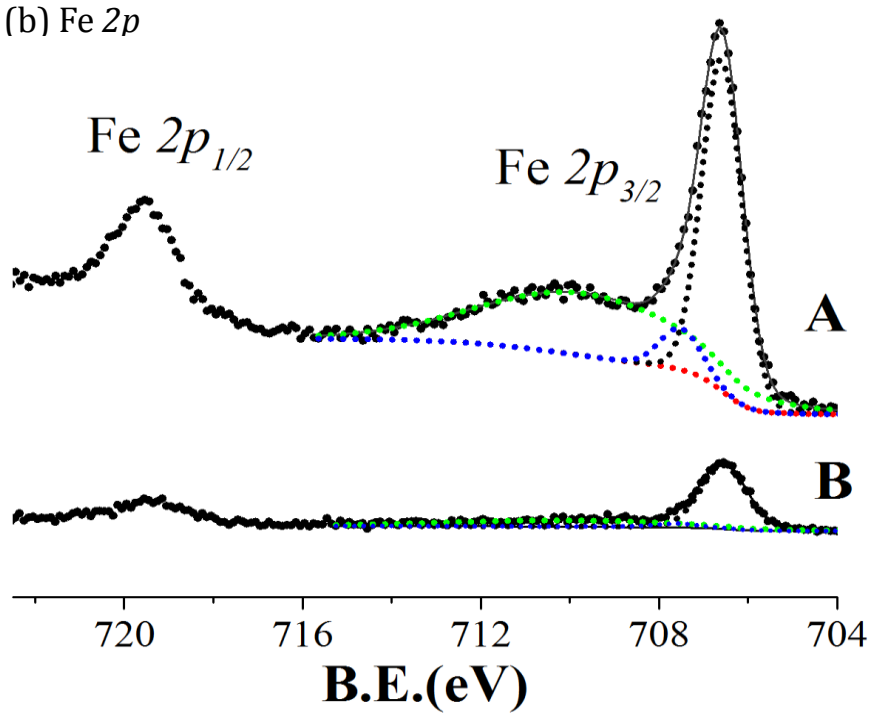

Figure 8c

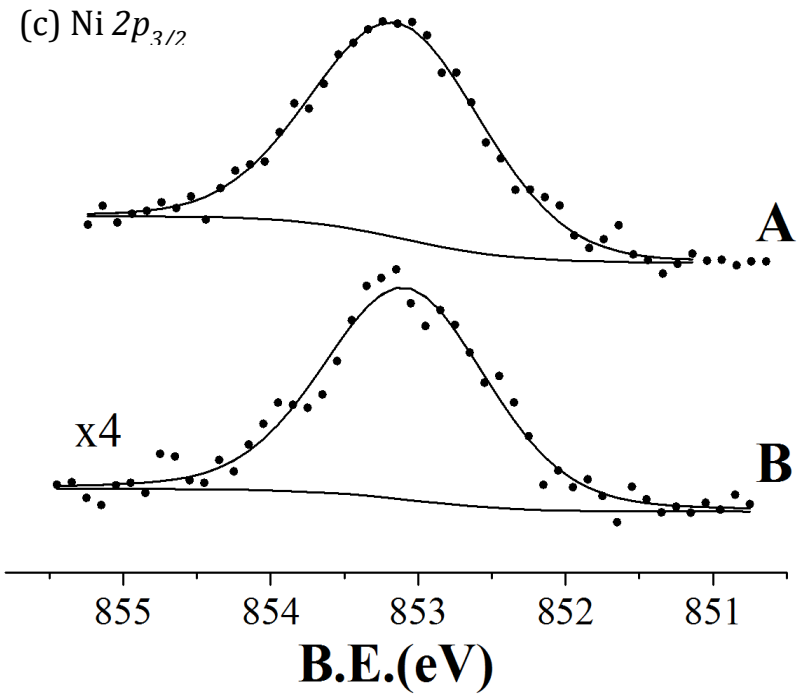

Figure 8d

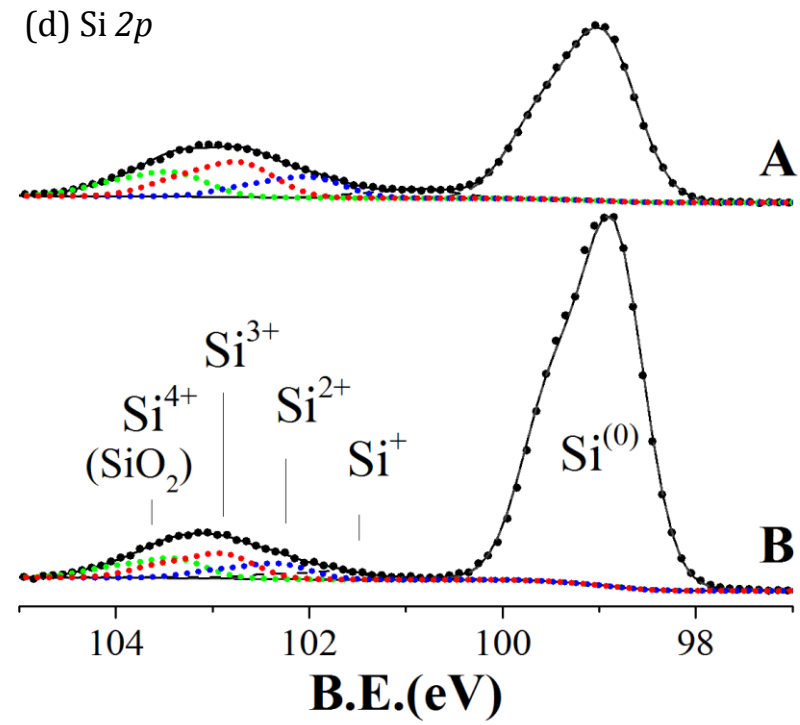

Suggested Layout of Figure 8

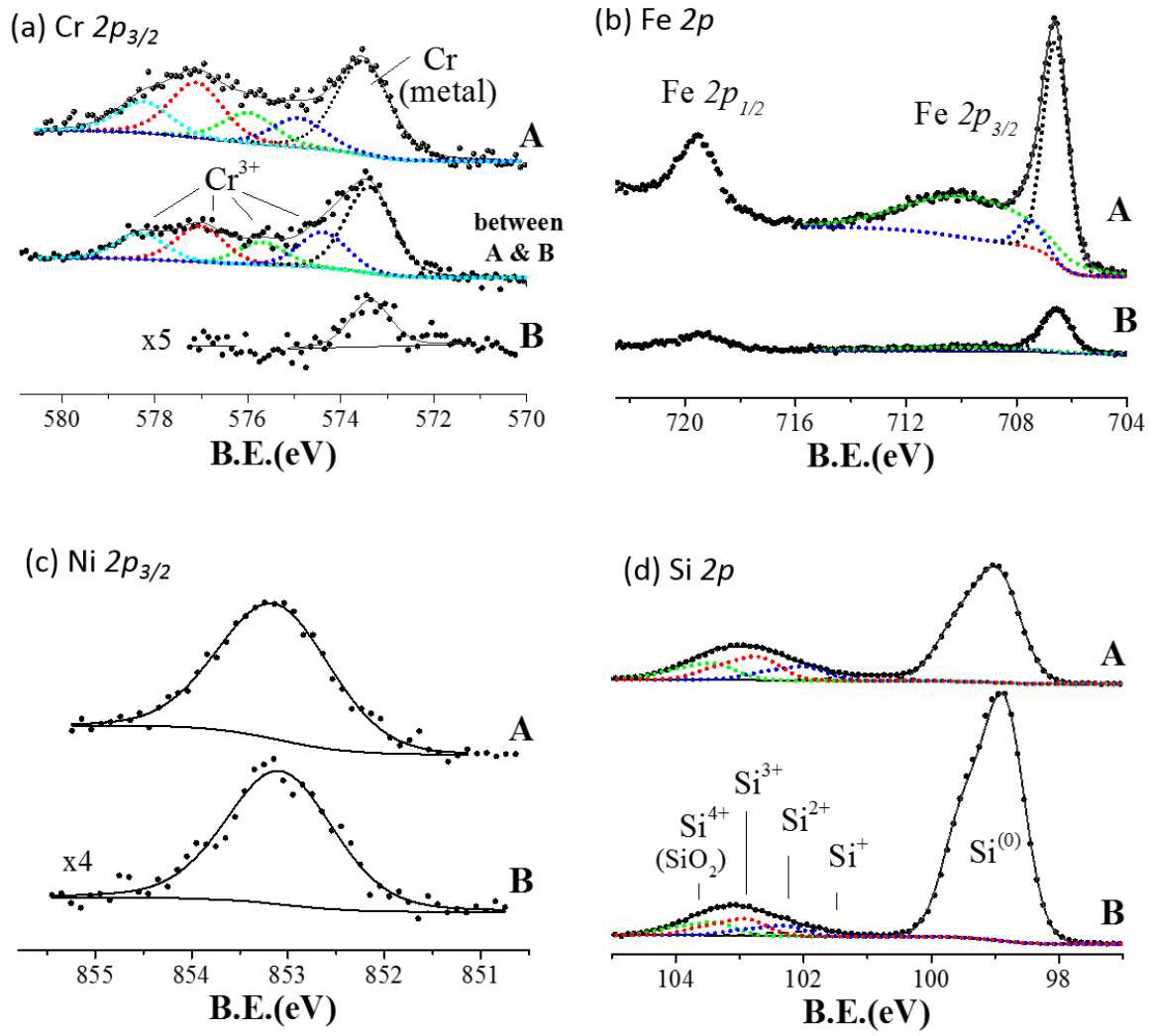

Figure 8

XPS core-level spectra, after irradiation with 1keV Ar^+ ions and co-deposition of SS atoms, at position A (nanocones) and B (nanoripples) on Si sample from Figure 3, as seen in Figure 1c.

(a) Cr $2p_{3/2}$ core level spectra. Notably for Cr, the nanocone region contains many more oxidation states than nanoripples. Cr(0) metal has a reported binding energy ~ 574.2 eV and other various Cr^{3+} states are seen at higher binding energies.

(b) Fe 2p core level spectra. Fe(0) metal $2p_{3/2}$ has a binding energy ~ 706.6 eV.

(c) Ni $2p_{3/2}$ core level spectra. Ni(0) metal $2p_{3/2}$ has a binding energy ~ 852.6 eV

(d) Si 2p core level spectra. Si(0) metal $2p_{3/2}$ has a binding energy ~ 99.4 eV.

Table 1.
Quantitative surface analysis via TXRF. Data quantified using multistandard (Cr, Mn, Fe, Ni & Cu) 10 μl of each solution pipetted on a SiO_2 sample Calibration curve constructed for each element, from which elemental concentrations for each sample position were determined. Detection limits are ~10^{11} atoms/cm^2 for light elements to ~10^9 atoms/cm^2 for heavier elements. Data presented was collected at position A (nanocones), between A and B (transitional nanocones) and position B (nanoripples).

	Cr [atoms/cm^2]	Mn [atoms/cm^2]	Fe [atoms/cm^2]	Ni [atoms/cm^2]	Cu [atoms/cm^2]
Position A	$2.1x10^{13}$	$3.5x10^{12}$	$6.8x10^{13}$	$2.1x10^{13}$	$6.2x10^{12}$
Position 1 between A & B	$4.8x10^{12}$	$3.2x10^{12}$	$1.4x10^{13}$	$7.6x10^{12}$	$8.1x10^{12}$
Position 2 between A & B	$4.7x10^{12}$	$1.7x10^{12}$	$1.5x10^{13}$	$3.9x10^{12}$	$2.3x10^{12}$
Position B	At detection limit (~$5.6x10^{11}$)	At detection limit (~$4.8x10^{11}$)	$5\ x10^{12}$	$8.1x10^{11}$	$5.8x10^{11}$

Table 2.
Semi-quantitative surface analysis via XPS. The elemental concentration is estimated using elemental sensitivity factors for all elements listed and by taking into account the transmission function for the electron energy analyzer. Data presented was collected at position A (nanocones), between A and B (transitional nanocones) and position B (nanoripples).

	Si (%)	O (%)	C (%)	Fe (%)	Cr (%)	Ni (%)	Ar (%)
position A	33±1	45±2	17±1	2.1±0.3	1.3±0.2	0.3±0.1	0.6±0.1
between A and B	42±1	38±1	18±1	1.3±0.3	0.4±0.1	0.15±0.05	0.4±0.1
position B	53±1	34±1	12±1	0.5±0.2	<0.1	<0.1	0.4±0.1